# Interface engineering by thiazolium iodide passivation towards reduced thermal diffusion and performance improvement in perovskite solar cells

*Manuel Salado [a,†], Michael Andresini [a,c,†], Peng Huang [a], Taukeer Khan [d], Fulvio Ciriaco [e],*

*Samrana Kazim,[a,b] and Shahzada Ahmad,[a,b*]*

[a] *BCMaterials-Basque Center for Materials, Applications and Nanostructures, Martina Casiano, UPV/EHU Science Park, Barrio Sarriena s/n, Leioa 48940, Spain.*
*Tel: +34 946128811 Email: shahzada.ahmad@bcmaterials.net*
[b] *IKERBASQUE, Basque Foundation for Science, Bilbao, 48013, Spain*
[c] *Department of Pharmacy - Drug Sciences, University of Bari "A. Moro" Via E. Orabona 4, Bari 70125, Italy.*
[d] *Department of Physics, Faculty of Science, Islamic University of Madinah, Prince Naifbin Abdulaziz, Al Jamiah, Madinah 42351, Kingdom of Saudi Arabia.*
[e] *Department of Chemistry, University of Bari "A. Moro" Via E. Orabona 4, Bari 70125, Italy.*
[†] *These authors contributed equally.*

**Abstract**

Interface engineering has become one of the facile and effective approach to improve solar cells performance, its long-term stability and retard unwanted side reaction. We have developed three passivating agents which can functionalize the surface and induce hydrophobicity by employing substituted thiazolium iodide (TMI) for perovskite solar cells fabrication. The role of TMI interfacial layers on microstructure and electro-optical properties was assessed for structural as well as transient absorption (TA) measurements. TMI treatment resulted into $V_{OC}$ and FF enhancement by reducing possible recombination paths at perovskite/HTM interface and by reducing the shallow as well as deep traps. These in turn allowed to achieve higher performance as compared to the pristine surface. Additionally, TMI passivated perovskite layer reduces considerably $CH_3NH_3^+$ thermal diffusion and degradation induced by humidity. The un-encapsulated perovskite solar cells employing TMI exhibited a remarkable stability under moisture levels (~50% RH) retaining ~95% of initial PCE after 800 h of fabrication, paving potential scalable endeavour.

**Introduction**

Hybrid inorganic-organic perovskite solar cells (PSCs) have emerged as promising photovoltaic (PV) material, yielding solar-to-electric power conversion efficiencies of 25.2 % in just a decade.[1] To optimize the performance, substantial progress has been made through compositional engineering.[2] Although methyl ammonium based perovskite is the most studied material, the mixed organic cations and halide anions gave stable and efficient solar cells.[3,4] For instance, the use of triple cations with inorganic cesium cation suppresses impurities and induces uniformity. In spite of such advantages, the cesium based absorber showed phase segregation[5] and poor atmospheric tolerance,[6] especially in high humidity conditions (~80% RH). Additionally, due to the layered structure of the devices, interfaces (physical interaction as well as energy level matching) between the different layers play a vital role in the final performance.[7] The fabrication of efficient and stable devices requires the strategy of having high $V_{OC}$ without sacrificing $J_{SC}$. Subsequently, efficient devices can be fabricated by minimizing the defect concentration associated with recombination processes in the material itself or by lowering the defect states at the interfaces.[8] Taking this in to account, the use of an engineered interface between the charge selective layer and perovskite has led to an improvement in the holes extraction as well as for the defects passivation on the perovskite surface.[9] The use of excess $PbI_2$ for the perovskite deposition resulted into the formation of a passivation layer that smoothened the top surface of absorber and led to an increment in the $V_{OC}$, however, the excess of $PbI_2$ was found to promote phase segregation. Due to the weak structure of perovskites, iodide anions are prone to volatility, while its diffusion induces irreversible degradation and destabilize the crystal structure. The inclusion of imidazolium iodide between perovskite and the hole selective contact to passivate the iodide vacancies in the crystal lattice was found an effective strategy to improve charge transport properties[10], and consequently, photovoltaic performance and durability was significantly improved. With an aim to develop new efficient passivating molecules to passivate the defect on the surface and interface between the perovskite/ HTM as well as hole extraction enhancement in PSCs, we rationally design three different substituted thiazolium iodide (TMI) salts, where the presence of sulphur atom

2

is supposed to play a pivotal role in interaction with perovskite's iodine atoms to enhance the perovskite-HTM interfacial contact and thus improves hole extraction.[11] Subsequently, we fabricated the PSCs using mixed cation/halide anion based perovskite and evaluated the PV performance by employing TMI based passivating agent and compared with control devices.

We elucidated the influence of passivated surface on PV parameters by modulating the passivating layer thickness as well as by changing TMI ring's substitution. In particular, mono or bi substitution of *N*-methyl thiazolium iodide hydrogen atoms with methyl group was explored, with the aim to modulate electron-donating properties of the layer and conferring hydrophobicity. Subsequently, it allowed to modulate hydrophillic character of the passivating layer, improving the intrinsic stability and thermal durability of PSCs.

**Results and discussion**

Three different substituted thiazolium iodides (Figure 1) have been synthesized and characterized as passivating agents with the aim to improve the thermal stability and opto-electrical properties, due to the interaction between the thiazolium and the perovskite surface. The three organic salts *N*-methyl thiazolium iodide (MIC2), 3,4-dimethyl thiazolium iodide (MIC3) and 3,4,5-trimethyl thiazolium iodide(MIC4) were synthesized through nitrogen methylation with iodomethane starting from the commercially available cost effective thiazoles (details in experimental part).

**Structural models and ab-initio computation**

We ran DFT B3LYP calculations for the determination of the energy of frontier orbitals of the salts with the aim to predict the efficacy of the passivation layer in the extraction of positive charge from the perovskite and the subsequent transmission to the Spiro-OMeTAD layer. As a result, HOMO-LUMO levels of the three salts calculated with a 6-311G basis set were found to be suitable for charge extraction purposes. Calculated HOMO levels were respectively -5.55 eV (**MIC2**), -5.41 eV (**MIC3**) and -5.23 eV (**MIC4**), while LUMO levels were -1.99 eV (**MIC2**), -1.92 (**MIC3**), -1.85 (**MIC4**) (Figure 1), depicting that these thiazolium salts present a large HOMO-LUMO energy gap

(approximately greater than 3.3 eV). The promising results signals that TMI could efficiently extract holes from the perovskite layer while, simultaneously, high LUMO levels could act as an electron barrier between anode and perovskite layer. With the aim to have an estimation of the binding energies of TMI salts adsorbed on perovskite surface, we also run the DFT PBE calculations based on the projector-augmented wave (PAW) method. In particular, TMI-perovskite binding energies were obtained by comparing the resulting energy of the TMI adsorbed on perovskite surface with the sum of the resulting energies of perovskite and TMI calculated with the same parameters. For MAPbI$_3$, a 2×2×3 supercell slab was generated with two surface cut along the (001) direction and a vacuum head-space of 20 Å. Figure 2 illustrates the abbreviated settings adopted for the upper and lower surface. The optimized geometries of **MIC2**, **MIC3** and **MIC4** from the previous calculations were used as input for the PAW calculations. In order to investigate the importance of k-points density, binding energies for **MIC2**, **MIC3** and **MIC4** on MAPbI$_3$ were calculated setting k-points density to (2.2.1) and (4.4.1). The resulting energies were found to be consistent, proving that k parameter set to (2.2.1) was sufficient for a correct modelling of the systems. We additionally ran calculations changing the cut-off energy for the plane-wave basis set from the default one (340 eV) to 400 eV and 450 eV. While calculated binding energies with 340 eV and 400 eV cut-off energies were found to be substantially different, we did not observe significant differences between 400 eV and 450 eV cut-off energy outputs. The estimated binding energy of **MIC2** was found to be the largest (-0.654 eV i.e. 63.1 kJ/mol), while **MIC3** and **MIC4** showed slightly lower interaction energies (respectively -0.338 eV and -0.257 eV). Therefore, the presence of a growing number of methyl substituents seems to affects the TMI / perovskite interaction, while the sulphur atom plays the pivotal role in coordinating perovskite ions. (Figure 1)
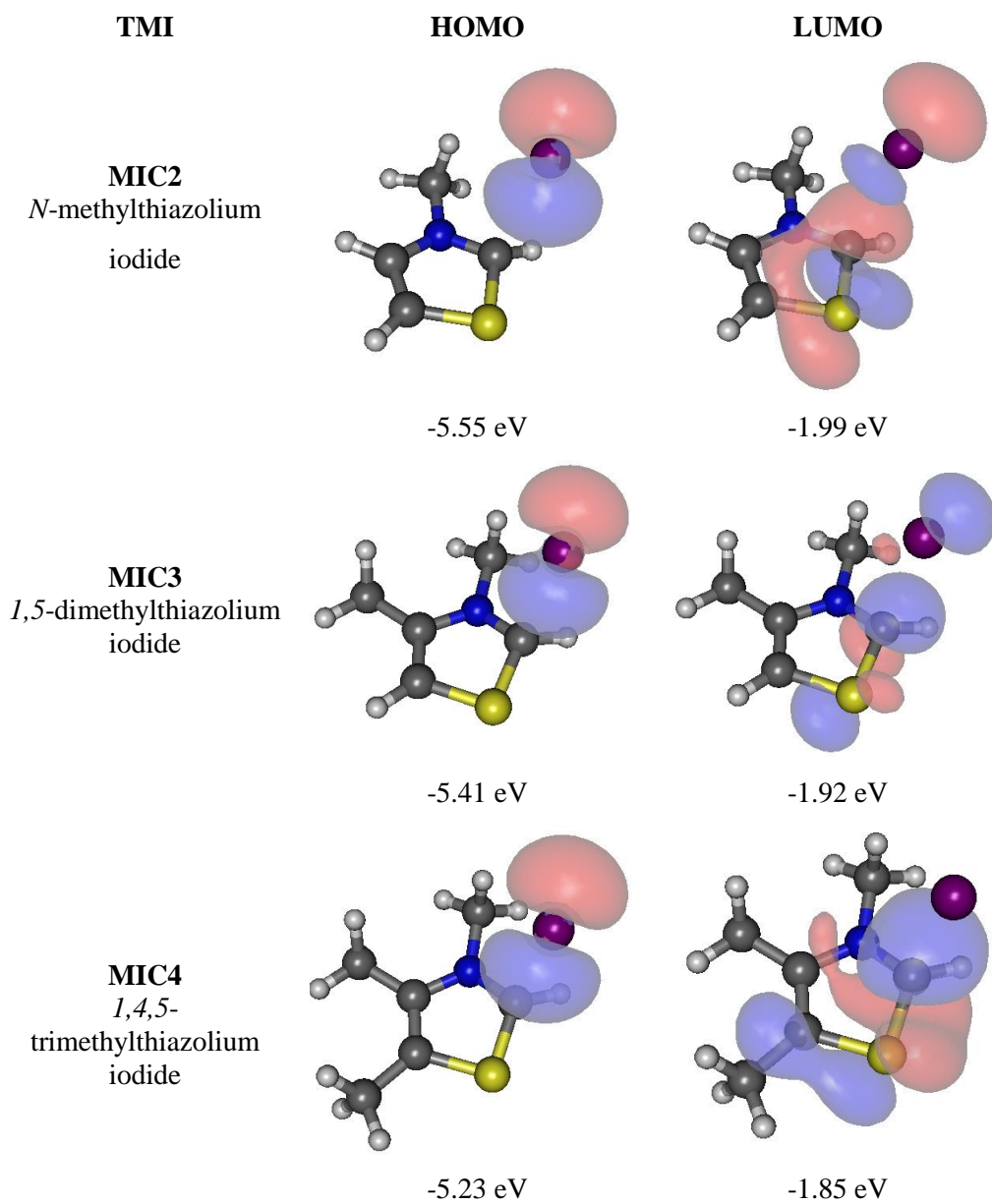
| TMI | HOMO | LUMO |
|-----|------|------|

**MIC2**
*N*-methylthiazolium
iodide

-5.55 eV          -1.99 eV

**MIC3**
*1,5*-dimethylthiazolium
iodide

-5.41 eV          -1.92 eV

**MIC4**
*1,4,5*-
trimethylthiazolium
iodide

-5.23 eV          -1.85 eV

**Figure 1.** Calculated molecular orbitals for **MIC2**, **MIC3** and **MIC4**.

**MAPI-MIC2**    **MAPI-MIC3**    **MAPI-MIC4**
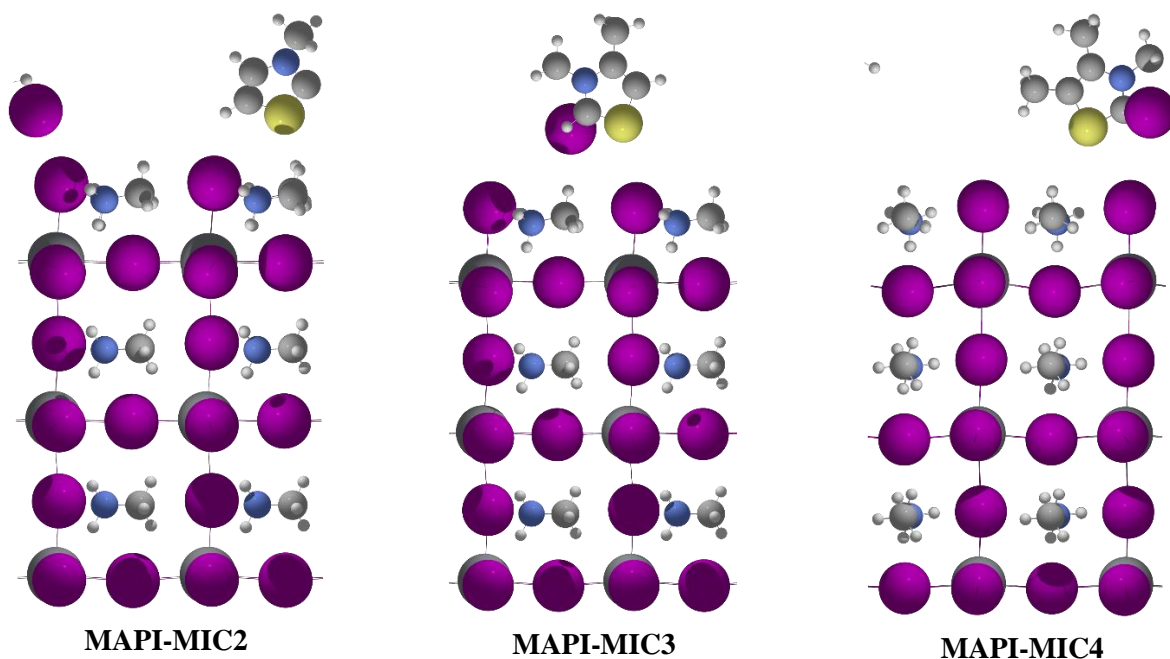
**Figure 2.** Output geometries of PAW calculations for **MIC2**, **MIC3** and **MIC4** (450eV cut-off energy, k (2.2.1).

## Characterization of the perovskite films

To elucidate the crystal structure of the passivating molecules, and possible changes induced in the methylammonium lead triiodide due to passivation, we carried out X-ray diffraction (XRD) experiments on the perovskite samples with and without TMI treatment (Fig. 3a,b). Expectedly, no noticeable changes in the main diffraction peaks (14.6º and 28.8º) of methylammonium lead triiodide with or without passivating treatment was found.[12] However, new diffraction peaks appeared after the passivation treatment. To further investigate whether the new peaks arises from passivating molecules crystallizing over the surface or from the formation of a organic thiazolium salt based perovskite, the diffractograms of TMI powders was also recorded (Fig. S2). The assessment of the diffraction patterns TMI and the new diffraction maxima generated after TMI passivation treatment, suggest the formation of $TMI_z$-$Pb_xI_y$ mixed type structure atop of $MAPbI_3$. Furthermore, we also discarded a symmetry reduction of the $MAPbI_3$ cubic structure due to partial substitution of MA by TMI cation. The peaks associated to the rhombic perovskite is not in accordance with the one generated after the deposition of TMI atop of $MAPbI_3$ layer. By discarding these two possibilities,

the experimental evidences pointing towards the surface modification induced by the presence of TMI.

The information elucidated from the new diffraction maxima generated after the TMI deposition is not sufficient for ab-initio determination of the passivated crystal structure. In order to gain further insights, we performed a full search of thiol-imidazolium bearing lead iodide structures in the Cambridge Structural Database, with a unique compound matching the MIC-1 characteristics.[13] Nevertheless, the simulated diffraction pattern derived from the 1-dimensional crystal structure reported is not in accordance with the position of the passivation layer maxima generated by the addition of MIC-1. Arguably, the XRD analysis suggests, the $TMI_z$-$Pb_xI_y$ passivation layers obtained after MIC-2, MIC-3 and MIC-4 usage have different crystal structures. Specifically in the case of MIC-3 and MIC-4, the presence of additional diffraction patterns suggest the possibility of layered type (2D) structures with interlayer spacing of 8 and 9 Å, respectively. This is in agreement with an expanded interlayer space due to the bulkier MIC-4 intercalation, in comparison to MIC-3, between the $PbI_2$ layers foreseen in layered 2D perovskites. For MIC-2 sample, the presence of several new peaks at low angles suggests a lower symmetric $TMI$-$PbI_3$ passivation layer structure. We ascribed this to the formation of a layered perovskite, which in literature is also termed as -2D perovskite atop of 3D perovskite surface, due to the large size of $C_3H_4NS$ ($r_{A,eff}$ = 320 ppm).[14] Such type of layered perovskite [15] will improve thermal durability and will induce an effective passivation effect, rather than the inclusion of TMI layer. Additionally, as aforementioned, the interaction with the perovskite would entail a better charge extraction, due to the interactions with the electron-rich sulphur atom from the thiazolium salts.
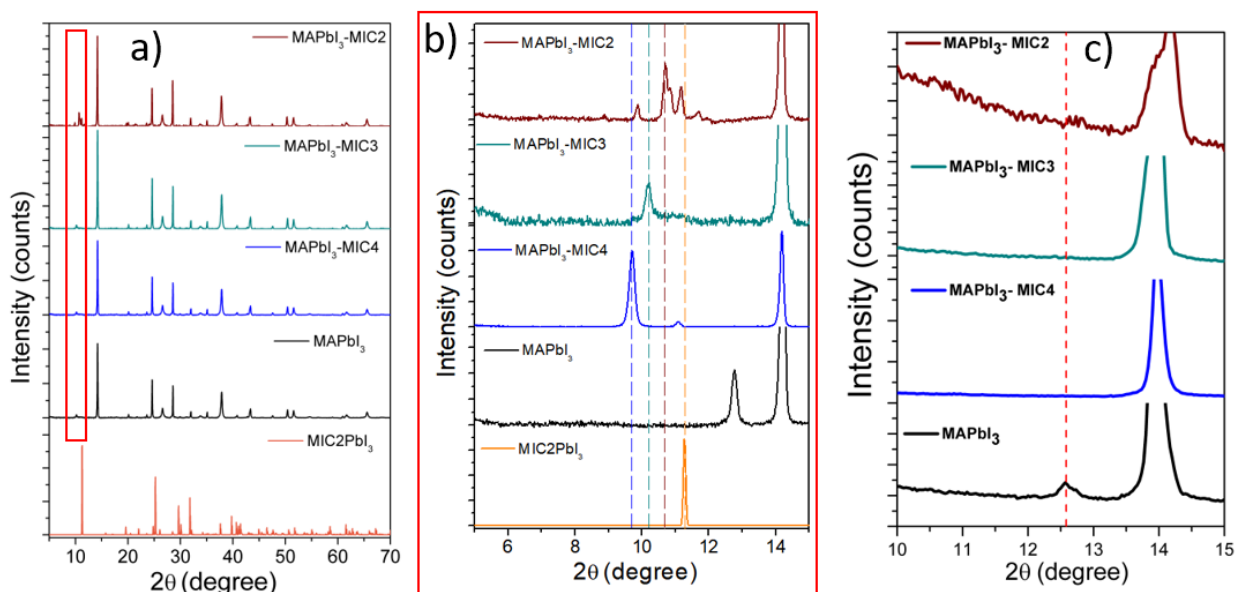
Figure 3. a) X-ray diffraction pattern of perovskite thin film and with passivation layer (MIC2, MIC3 and MIC4), b) zoom-in of the low angle peaks after passivation (red rectangle in 2a) indicating the main reflection peaks of the different passivation layers and c) diffractograms at 140ºC. (red line indicates the presence of $PbI_2$ characteristic peak).

Arguably, the use of a passivation layer at the perovskite / HTM interface improves the charge extraction from the perovskite and prolong the lifetime of the devices.[10,16] In the past,[10,17] an improvement in the $V_{OC}$ and the fill factor (FF) of perovskite based devices was reported, due to fine energy level alignment between layers that improves the charge extraction. Remarkably the stability was also improved with the utilisation of fluorinated based compounds which improves the hydrophobicity of the perovskite surface, repelling moisture and increasing its environmental tolerance.[18,19] However, in operational conditions, besides humidity, high temperature represents another main factors that entails a fast degradation process.[20] $CH_3NH_3PbI_3$ crystals are reported to suffer from thermal diffusion at 135ºC, when methyl ammonium cation scatters from the crystalline network.[21] This effect results into an irreversible process, towards the formation of the initial precursors ($PbI_2$ + $CH_3NH_3I$). Thus, thermal stability of the passivated perovskite layers was monitored by temperature dependence X-ray diffractograms. For this, the samples were heated at varying temperatures (30 ºC, 50 ºC, 100 ºC, 120 ºC, 140ºC, 150ºC) and cooled down (Figure S3) to

investigate irreversibility in the degradation. It can be deducted from Figure 3c, TMI passivated devices showed higher thermal stability, even at 150 ºC in the case of MIC4 usage. This behaviour is in accordance with the TGA measurements of substituted TMI (Figure S4) which are found to be thermally stable above 220ºC. Perovskite microstructure was studied by scanning electron microscopy (SEM) (Fig. S5). We found that TMI salts covers the perovskite surface, particularly, the highly substituted TMI covered the grain boundaries entirely. TMI passivating layer reduces the surface roughness (visualized from the SEM images) between the grain boundaries and the surface. Depending on the composition of the perovskite, the hydrophobic character can reduces the degradation by water inclusion in the perovskite layer. Mixed perovskites with cesium cation in their compositions, presents higher stability than methyl ammonium based ones. However, phase segregation in mixed perovskites is still unclear, and can limit its up-scaling purposes.[5] To evaluate the hydrophobic property induced by passivating layer, contact angle measurements were carried out on perovskite films treated with the TMI salts, together with a control sample. Expectedly, the deposition of the passivation layer induces an increase in the contact angle value (>80º) compared to reference sample (70º) (Figure S6). Thus, a better interface protection against humidity can be conferred. Optical behaviour was analysed by UV-Vis absorbance (Figure 4a) to study possible changes in the optical band-gap for the passivated perovskite. We noted the optical absorption spectra of TMI treated perovskites are similar to the pristine $MAPbI_3$, signalling that TMI salts have negligible effect on light harvesting properties. The strong PL emission band centred at 773 nm was observed for pristine $MAPbI_3$ (MAPI) deposited on glass and excited at 460 nm from glass side. A significant decrease in PL intensity was noted for TMI treated perovskite surface. Expectedly, MAPI treated with TMI shows blue shifting in PL peak from 773 nm to 769 and 768 nm for MIC2 and MIC3 respectively. The PL quenching of the passivated perovskites suggest their assistance in hole extraction by these TMI salt, as indicated by their higher HOMO level compared to the MAPI valence band. In addition to this, higher FF factor were obtained for the solar cells fabricated with MIC2 and

MIC3 treated perovskite.[22,23] The blue shift of the PL emission in TMI passivated perovskites can be ascribed to the reduced number of trap density of state, as a result of passivating trap states in the bulk as well as on the surface/grain boundaries of the perovskite. These results are in accordance with admittance spectroscopy measurement, which depicts an increment in the recombination resistance of the device at $V_{OC}$, as shown by the DOS value calculated using temperature dependence admittance spectroscopy. These results show that the alkyl chain of TMI can fill the voids (defects) on the grain boundaries surface and interface of perovskite and HTL layer, thus passivating the perovskite surface. Similar blue shifting behaviour was also observed for other organic molecules used for passivating the perovskite.[10,24–29]

In order to investigate the charge carrier dynamics in TMI passivated perovskite, thin film was deposited on quartz substrate and femtosecond-transient absorption spectroscopy (fs-TAS) was performed. The lower pump excitation energy density ~4 μJ /cm$^2$ was used to avoid auger recombination and excitation energy density was constant for all the samples having the same perovskite thickness, ensuring that a similar charge carrier density is generated. Fig 4b&c show the fs-TAS spectra of pristine MAPI and MAPI treated with MIC2 film using pump excitation wavelength of 510 nm and probed at different delay time by a probe pulse of white light continuum. Three different spectral regions were observed, a negative photo induced bleaching peak was observed at 760 nm and two positive photo induced absorption peaks were observed at both sides of the 760 nm band i.e. below 720 and >780 nm. The photo induced negative bleaching peak (PB) observed at 760 nm (position of $E_g$, optical band gap) can be allotted to the ground state bleaching due to the excitons absorption, which leads to band filling[30,31] i.e. the presence of band gap carriers or excitons. The photo induced positive peak (PB) below 720 and >780 nm can be attributed to the absorption of the excited transient species.[32] As reported in our other reports, the observed bleaching band on a time scale of a few picoseconds (ps) may corresponds mostly to the exciton dynamics. As mentioned before, we used 510 nm excitation, which is not sufficient to excite charge carriers in the

second valence band. Consequently, the hole cooling is absent and therefore the rising of the bleach at 760 nm ($\tau$=0.14 ps) reflects directly the exciton formation. Electron cooling is reflected by the decay of transient around 815 nm (0.32 ps) and the growth of the positive contribution at wavelengths below 720 nm (0.2-0.3 ps). Fig. 4d shows the comparison of kinetics profile of 760 nm bleaching peak at ~4 µJ /cm$^2$. The observed exciton dynamics in the first 5 ps is very similar in the pristine and TMI treated perovskite films, which exhibited the same TAS decay lifetime of 0.14 ps by fitting the single exponential function. We suggest that the dynamics of free carriers are an intrinsic property of the perovskite and therefore, these processes are not influenced by the passivation layer. Moreover, PL quenching as well as TA measurements indicate that TMI treatment suppresses the surface non-radiative recombination defects.
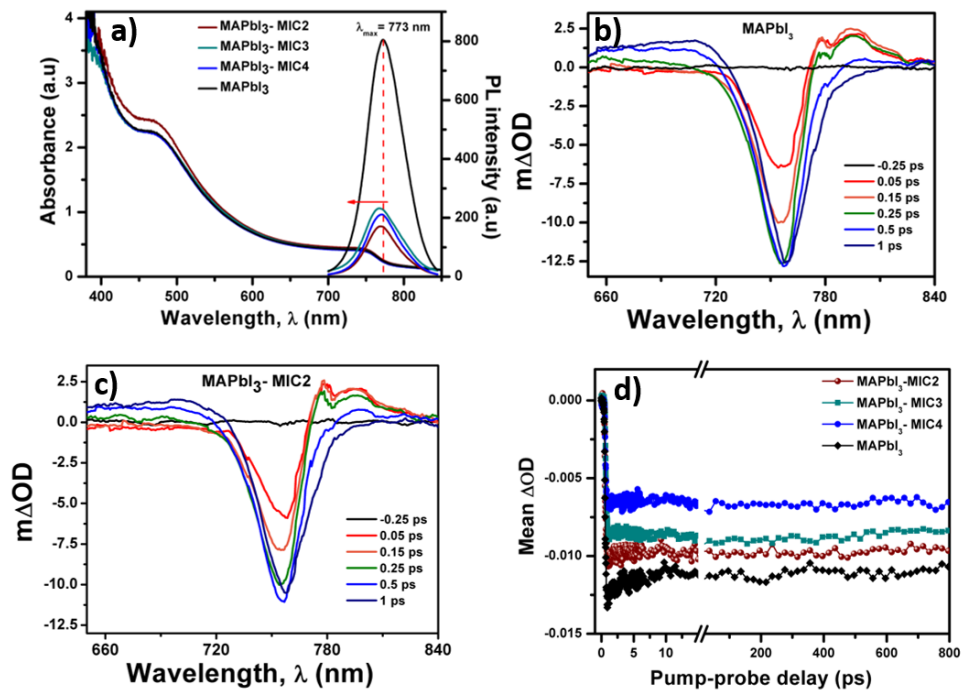


Figure 4. a) Absorption spectra and Steady state PL emission measured at 460 nm excitation of pristine perovskite and TMI treated, b,c) fs-Transient absorption spectra of pristine MAPbI$_3$ perovskite and MIC2 passivated perovskite film excited at 510 nm with the excitation energy 4uj/cm$^2$ at pump-probe delay from 0 to 1ps and d) kinetic delay for photo bleaching probed at 760 nm of the perovskite film without and with TMI treatment.

## Device fabrication and characterization

Considering that TMI can efficiently passivate the surface defects in the perovskite layer, we fabricated devices with FTO/b-TiO$_2$/meso-TiO$_2$/MAPbI$_3$, Cs$_{0.05}$MA$_{0.15}$FA$_{0.85}$Pb(I$_{0.85}$Br$_{0.15}$)$_3$ and MA$_{0.33}$FA$_{0.66}$PbI$_3$ /Spiro-OMeTAD/Au structure. The thicknesses of the electron transport layer TiO$_2$, the perovskite layer and the hole transport layer Spiro-OMeTAD was in total about 0.8 μm, (150 nm, 500 nm and 140 nm, respectively) (Fig. 5a). The dependence of TMI on the device performance by the usage of MIC2, MIC3 and MIC4 (Table S1a and b) was competitive and represents significantly increased PCE when the perovskite was treated with a substituted thiazolium iodide (MIC3) as compared to control sample. Devices fabricated with MIC4 as passivating agent showed an increment in the series resistance (Figure 5c). We speculate that due to the methyl substitutions, complete solubility in 2-propanol was difficult to achieve, resulting into aggregates which interacts with Spiro-OMeTAD to act as recombination sites. Due to this, the device performance drops with higher substituted TMI salts even though the recombination rate was low. (Figure 6).
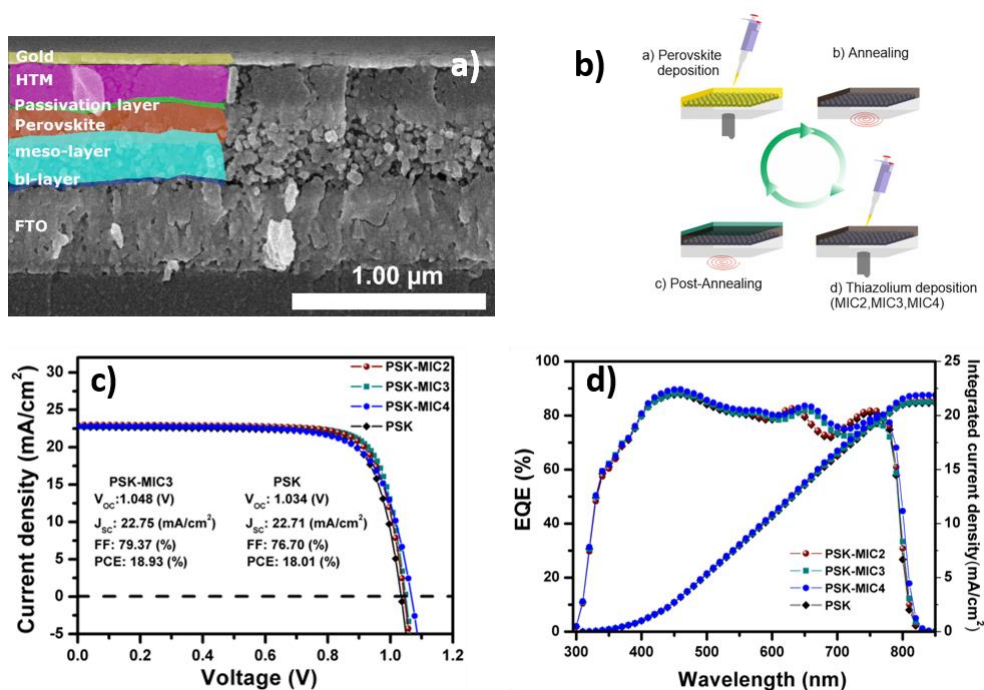
Figure 5. a) Cross-section SEM image, b) schematic process for deposition of passivation layer, c) *J-V* curves of surface passivated and pristine device and d) EQE and integrated current density of devices. The device structure was FTO/SnO$_2$/ MA$_{0.33}$FA$_{0.66}$PbI$_3$ /Spiro-OMeTAD/Au.

In order to evaluate the beneficial effect of the TMI passivation in devices, we tested different perovskite compositions (CH$_3$NH$_3$PbI$_3$, Cs$_{0.05}$MA$_{0.15}$FA$_{0.85}$Pb(I$_{0.85}$Br$_{0.15}$)$_3$, MA$_{0.33}$FA$_{0.66}$PbI$_3$) and different architectures {mesoscopic (TiO$_2$) and planar (SnO$_2$)} to estimate their PV properties. After optimization of the TMI-treated device, we obtained the best device with an efficiency of 18.93%, which gave a $V_{OC}$ of 1048 mV, $J_{SC}$ of 22.75 mA cm$^{-2}$ and a fill factor (FF) of 79.37% (Fig. 5a). The integrated current density from the external quantum efficiency (EQE) was 21.5 mA cm$^{-2}$ (Fig. 5b), which is in agreement with data obtained from the measurement of *J-V* curves reported in this study. As previously reported [10], even in this case the optical band-gap remain unchanged after deposition of the passivation layer , and it can be stated that the low dimensional perovskite formed atop of the 3D perovskite does not affect the optical properties of the material. Furthermore, EQE decreases to half the peak value and the differential of the EQE (Fig. S7a) suggests that the absorption threshold is 1.61 eV. This value is consistent with the result obtained from the differential of absorption (Fig. S7b). The PCE statistics validates the reproducibility of our results suggesting the improvement in the performance of PSCs (Fig.S8 and Fig.S9).

Charge accumulation and hysteresis behaviour in PSCs have been attributed to the interactions between layers.[33] Although the identification of the process involved can be complex, it is possible to explain the processes occurring in the bulk of perovskite with the use of admittance spectroscopy.[34] Recently, the importance of conduct analysis to identify recombination and transport processes in the devices was highlighted.[35] We have employed electrochemical impedance spectroscopy (EIS), to analyse the devices with different passivation materials and MAPI as examples to avoid complications in the analysis of EIS data (Figures S11, S12 and S13). According to the

microstructure, (XRD, SEM) and opto-electrical (*J-V*, EQE, TA) characterization, a clear interaction between the passivation material and perovskite was noted, which will have its bearing in the charge recombination and transport inside the devices. Figure 6, illustrates the recombination resistance at different photo-voltages. A plain influence of the passivation layer on the recombination process due to a filling of grain boundaries as well as defects could be observed, which is accordance with previous reports.[16] Recombination resistance, close to the open circuit voltage, is higher when MIC4 was used as passivation agent, which suggests a reduction of the non-radiative recombination defects. We calculated the ideality factors obtained from the slope $R_{rec}$ vs V indicating a different recombination mechanism (from bulk β~0.5-0.6 to surface β<0.5).[36] According to the figure, non-passivated samples showed a trap-state recombination, meanwhile a progressive change in the slope was observed when substituted thiazolium salt were used as passivating agent.
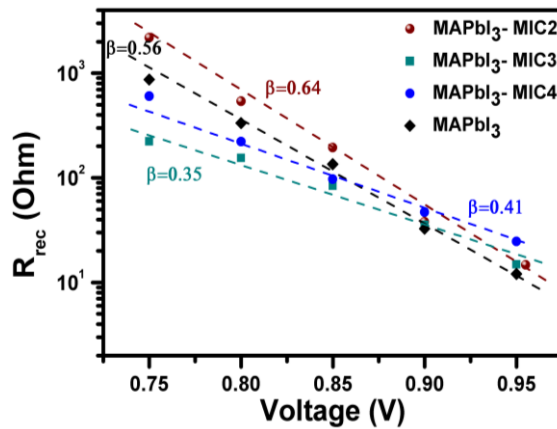


Figure 6. Recombination resistance vs. voltage obtained at room temperature from impedance spectroscopy experiments.

We suggest that the improved thermal resistance together with the hydrophobic character of the passivation layer, induce a better long-term stability of the perovskite devices.[37] We assessed the long-term device stability for 800 h (Fig. 7a). In particular, we periodically tested the devices which were kept under dark conditions and relative humidity (RH~ 50-60%). It is worthy to note, that the control device (non-passivated) presented a decay in the efficiency as well as in the EQE (Figure S10). On the contrary, TMI treated samples showed reduced losses in efficiency. Moreover, we investigated the device stability under continuous light soaking at the maximum power point (25 °C,

100 mW cm$^{-2}$) and we found that there is no obvious decrease in device performance (Fig. 7b), except for the not passivated ones, where a loss of almost 20% of the initial efficiency was observed. Our results suggest that the long-term stability of TMI-based devices is very competitive and suitable for applications under real operation conditions.
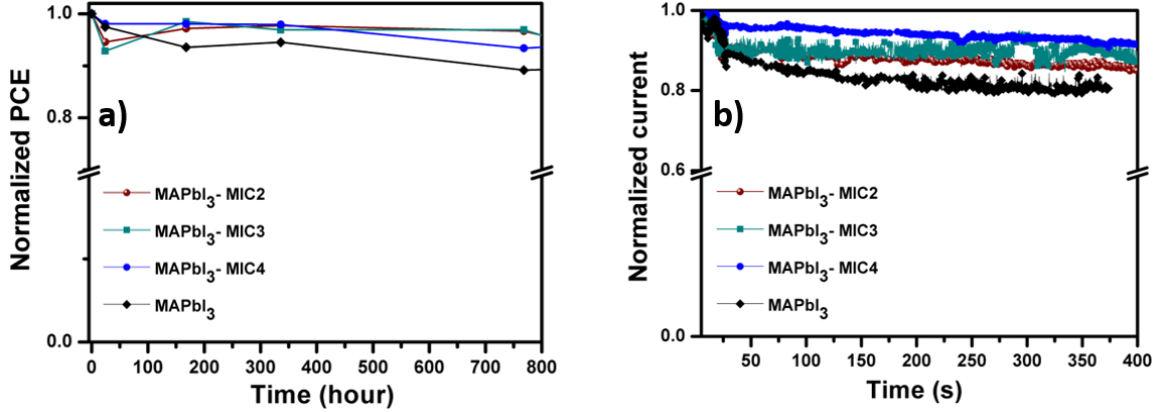


Figure 7. a) Evolution of PCE with time under atmospheric humidity conditions (~60% RH) over 800 h and b) photo-stability at MPP under continuous illumination (1 sun AM 1.5 (1000 W/m$^2$)) for un-encapsulated devices.

**Defect Spectroscopy**

To analyse the effect of TMI passivation on distribution of trap density in MAPbI$_3$ absorbing layer, we performed temperature dependence admittance spectroscopy and Mott-Schottky analyses. We first measured the temperature dependent capacitance as a function of frequency. From the derivative of the capacitance spectrum (SI Figure S16) we determined the frequency ($f_{peak}$) of peak emission rate of electrons from a trap state located below $E_T$ to the LUMO edge $E_{LUMO}$ as depicted schematically in Figure 9. From the slope of Arrhenius plot, $\ln\left(\dfrac{f_{peak}}{T^2}\right) vs. \dfrac{1}{T}$, the value of activation energy E$_A$, and attempt to escape frequency $\upsilon_0$ were deduced through the relation:[38]

$$\ln\left(\frac{\nu_0}{T^2}\right) = \ln(\beta) - \frac{E_A}{k_B T} \qquad (1)$$

where β is a proportionality constant, T is the temperature and k$_B$ is the Boltzmann constant. The calculated activation energy for each device are presented in Table 1. The defect activation energy of all the devices have similar value and found to be close to 90 meV.

The Mott-Schottky analyses was made to measure the value of built-in-potential $V_{bi}$, and depletion layer width W at perovskite/HTM interface. A Mott-Schottky plot is a capacitance – voltage (*C-V*) graph at a frequency where device capacitance is frequency-independent. In the depletion region, the total charge density is determined only by the density of immobile dopants N and can be considered an ideal parallel plate capacitor. The width of the depletion layer is related to the capacitance C through the relation $C = \dfrac{\varepsilon \varepsilon_0 A}{W}$. The built-in potential ($V_{bi}$), doping density of immobile ions N of perovskite layer is related to the capacitance through the relation:[39]

$$\frac{1}{C^2} = \frac{2}{\varepsilon \varepsilon_0 qN}\left(V - V_{bi} - \frac{k_B T}{q}\right) \qquad (2)$$

Mott-Schottky plot of fabricated devices at 10 kHz is shown in Figure 8a. The values of $V_{bi}$ was extracted from the intercept on bias axis and then N was calculated from the slope of the linear region using equation (2). The depletion width W corresponding to zero bias was calculated from the equation $W = \sqrt{\dfrac{2\varepsilon \varepsilon_0 V_{bi}}{qN}}$. We can deduct from Table 1 that the depletion width of perovskite layer was increased from 59 nm for device without any passivation layer to 63 nm for MIC3 passivation and 69 nm for MIC4 passivation layer. Due to the increase in depletion width, the built in potential of passivated devices was improved from 0.75 V for device without any passivation layer to > 1.1 V for passivated devices. The increased $V_{bi}$ value enhance the charge transfer at the perovskite/HTM interface.
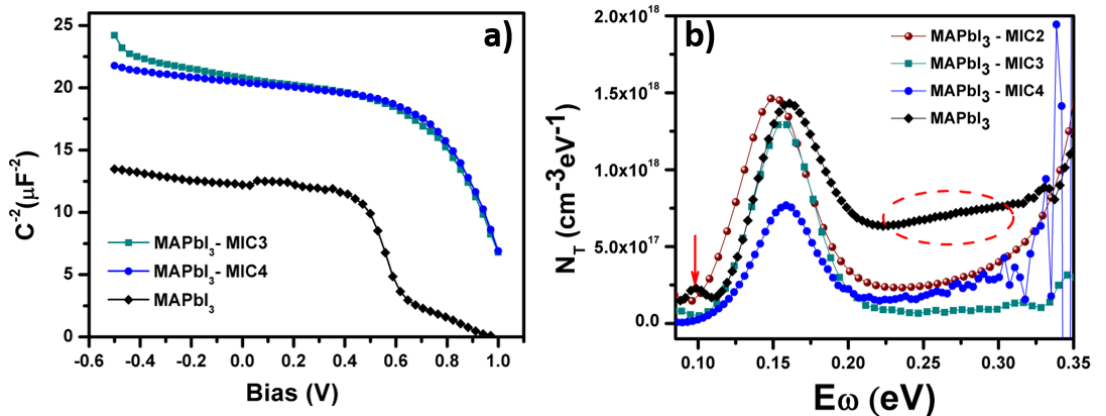
Figure 8. a) Mott−Schottky analysis and, b) trap density of states (NT) of all devices at 300 K.

The trap density profile were calculated from the equation[40]

$$N_T = \left(-f\frac{dC}{df}\right)\frac{V_{bi}}{qWk_BT} \qquad (3)$$

and are presented in Figure 8b. E$\omega$ represents a demarcation energy and was calculated from the

equation $E_\omega = k_BT\ln\left(\dfrac{\beta T^2}{\omega}\right)$. It can be observed from the Figure 8b that the traps distributed through

a Gaussian curve, and thiazolium passivation significantly reduced the overall trap density of states

in the band gap of perovskite layer (highlighted by dotted ellipse). The peak value of DOS was also

reduced from $1.44\times10^{18}$ (eV cm$^3$)$^{-1}$ for reference device to $6.08\times10^{17}$ (eV cm$^3$)$^{-1}$ for MAPI-MIC4.

Moreover, the trap density profile of reference device showed an additional peak around 0.1 eV which

corresponds to shallow traps with a density of $2.46\times10^{17}$ (eV cm$^3$)$^{-1}$. This peak is almost diminished

in the passivated devices, further confirming that TMI passivation represents an effective strategy to

reduce the shallow as well as deep traps at the interface of perovskite absorbing layer and HTL.

Table 1. Device parameters deduced from admittance spectroscopy and Mott-Schottky plot.

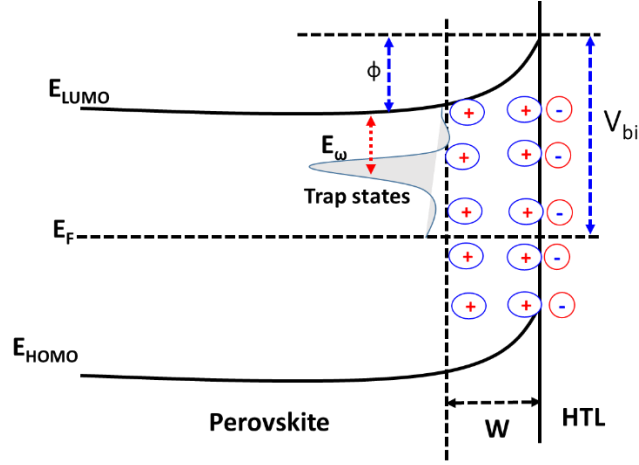| Parameters | MAPI-MIC2 | MAPI-MIC3 | MAPI-MIC4 | MAPI |
|---|---|---|---|---|
| Activation Energy E$_A$ (meV) | 92.72 | 90.73 | 89.00 | 90.58 |
| Depletion layer width W (nm) | - | 63 | 69 | 59 |
| Built-in-potential V$_{bi}$ (V) | - | 1.18 | 1.14 | 0.75 |
| Doping density N cm$^{-3}$ | $1.0\times10^{17}$ | $7.54\times10^{17}$ | $6.08\times10^{17}$ | $6.08\times10^{17}$ |
| Peak value of traps DOS (eV cm$^3$)$^{-1}$. | $1.47\times10^{18}$ | $1.29\times10^{18}$ | $7.72\times10^{17}$ | $1.44\times10^{18}$ |
| Peak position of traps density (eV) | 0.151 | 0.157 | 0.159 | 0.161 |

Figure 9. Band diagram of a p-i-n junction, where φ is the band bending at the junction, Ec is the conduction band, $E_{LUMO}$ is the LUMO level, $E_F$ is the Fermi level, W is the width of the depletion layer, $V_{bi}$ is the built-in field, and Eω is the demarcation energy that separates traps that respond to Vac at frequency ω from those that do not.

## SCLC Results

Charge carrier mobility (μ) and density of traps ($n_{trap}$) in the fabricated devices was extracted via evolution of the space charge limited current (SCLC). At low applied bias (Fig. 10.) the *J-V* characteristics follow Ohm's law (red line). The electrical conductivity (σ) was evaluated from the ohmic region through the relation: $\sigma = JL/V$ , where L is thickness of thin films. The conductivity of pristine device was calculated to be $3.76 \times 10^{-7}$ S/cm, while the device with *N*-methylthiazolium iodide passivation (MAPI-MIC2) gave conductivity value of $4.59 \times 10^{-7}$ S/cm. On further increase of applied bias, the injected carrier starts to fill the traps and when applied bias reached at the onset voltage $V_{TFL}$ , all traps states filled from injected carriers and *J-V* characteristics starts to follow Child's law (orange line) as represented by equation: [41–43]

$$J = \frac{9}{8}\varepsilon\varepsilon_0\mu\frac{V^2}{L^3}$$

where ε is the dielectric constant of perovskite layer and $\varepsilon_0$ is the permittivity of free space. From Child's region, we extracted the mobilities of all devices and presented in Table 2. All devices exhibits similar values of mobilities of $9.86 \times 10^{-4}$ cm$^2$/V s for MIC2, $7.25 \times 10^{-4}$ cm$^2$/V s for MIC3, $9.59 \times 10^{-4}$

cm$^2$/V s for MIC4, and $1.11 \times 10^{-3}$ cm$^2$/V s for reference device. The trap density n$_{trap}$ was estimated using following relation:

$$n_{trap} = \frac{2\varepsilon\varepsilon_0 V_{TFL}}{eL^2}$$

From these results, it is evident that the devices with TMI passivation layers showed fewer defects as compared to reference device. The free carrier concentration in perovskites was evaluated through the relation: $n_c = \sigma/_{e\mu}$ and for pristine devices, it was estimated to be $2.12 \times 10^{15}$ cm$^{-3}$, whereas it shows enhancement for the devices with TMI interfacial layers. This might be due to decrease of trap density in these devices which results in increase of free carrier density.
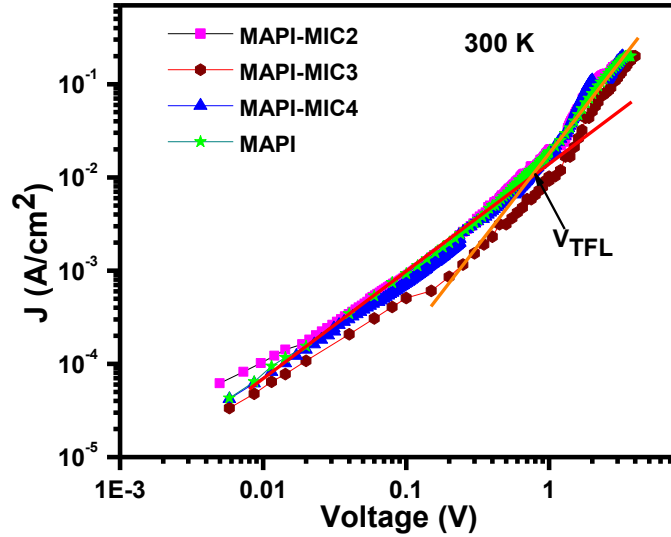


Figure 10. Dark *J-V* characteristics of devices with various TMI based passivating agents at 300 K.

Table 2. Electrical parameters extracted from SCLC measurements.

| Device | σ (S.cm$^{-1}$) | μ (cm$^2$V$^{-1}$s$^{-1}$) | n$_C$ (cm$^{-3}$) | n$_{trap}$ (cm$^{-3}$) |
|---|---|---|---|---|
| MAPI-MIC2 | $4.59 \times 10^{-7}$ | $9.86 \times 10^{-4}$ | $2.91 \times 10^{15}$ | $1.17 \times 10^{16}$ |
| MAPI -MIC3 | $2.60 \times 10^{-7}$ | $7.25 \times 10^{-4}$ | $2.24 \times 10^{15}$ | $1.30 \times 10^{16}$ |
| MAPI -MIC4 | $3.49 \times 10^{-7}$ | $9.59 \times 10^{-4}$ | $2.28 \times 10^{15}$ | $1.29 \times 10^{16}$ |
| MAPI | $3.76 \times 10^{-7}$ | $1.11 \times 10^{-3}$ | $2.12 \times 10^{15}$ | $1.48 \times 10^{16}$ |

To conclude, substituted thiazolium iodides have been employed as passivating agent to allow interface engineering and minimizing the defect concentration by means of passivation. We noted improved thermal stability and opto-electrical properties due to the interaction between the thiazolium salts and the perovskite surface. The reported simplistic method towards passivation of the perovskite surface allowed a significant reduction in defects and suppression of recombination phenomena. Moreover, the straightforward and cost-effective synthesis of thiazolium based compounds, together with their integration in device towards improved charge extraction, is presented. Deposition of substituted *N*-methyl thiazolium iodide salts resulted into improved performance as compared to the control devices and was found to be compatible with high performance device fabrication. Additionally, passivating layer inclusion reduced long-term instability of un-encapsulated devices. Simulations studies suggest that the presence of a higher number of methyl substituents affect the thiazolium iodide-perovskite interaction, while the sulphur atom plays the pivotal role in coordinating perovskite ions. We elucidated the underlying mechanism for a rational passivation layer development, which could facilitate further investigations towards performance enhancement of perovskite based materials for energy application.

**Experimental methods**

*Solar cell device fabrication*

Perovskite solar cells were fabricated on FTO (NSG10) substrates previously cleaned by a sequential treatment in the ultra-sonicator bath in a 2% Hellmanex solution, acetone and isopropanol, followed by UV ozone treatment for 20 min. Then samples were heated then to 500°C and a compact blocking layer of $TiO_2$ was deposited onto the FTO glass substrate by spray pyrolysis, using a dilution 1/19 ml of titanium (IV) diisopropoxide bis(acetylacetonate) solution in ethanol keeping them for 30 min. After the samples were at room temperature, a mesoporous dispersion of $TiO_2$ nanoparticles (30 NRD from Dyesol) in ethanol was spun-coated at 2000 rpm (1000 rpm/s acceleration) for 30s, followed by a progressive heating step till 500 °C for 30 min. Stoichiometric precursor solutions (1.25 M) were prepared, by mixing MAI (Sigma Aldrich) and $PbI_2$ (TCI) in *N,N'*-dimethylsulfoxide (DMSO) and kept under stirring at 70 °C overnight in order to dissolve completely $PbI_2$. The perovskite and HTM films were prepared inside an argon glove box under moisture and oxygen controlled conditions ($H_2O$ level:1 ppm and $O_2$ level:10 ppm). The perovskite layers were fabricated by using a two-steps spin-coating process, first step 1000 r.p.m. for 10 s; second step 3500 r.p.m for 30 s. During the second step 110 µl of chlorobenzene were poured onto the films 10 s prior to the end of the program,

and then substrates were annealed at 100 °C during 40 min. For planar PSCs, The $SnO_2$ layers as ETMs were fabricated by spin-coating on the pre-cleaned ITO substrate at 2500 rpm for 30 s using the diluted $SnO_2$ aqueous colloidal dispersion with the concentration of 2.5 wt%. The $SnO_2$ films were annealed in air at 150 °C for 15 min. The perovskite films were obtained by the two-step deposition method. In short, $PbI_2$ (1.3 M) containing was dissolved in 1 mL of DMF and DMSO (ratio = 9.5: 0.5) solution at 70 °C. Then the solution was spin-coated on the $SnO_2$ substrate at 2000 rpm for 30 s, and a mixture solution of FAI : MABr : MACl (60 : 10 : 10 mg in 1 mL IPA) was spin-coated on the $PbI_2$ substrate at 2000 rpm for 30 s. The as-prepared films were annealed at 150 °C for 15 min under 30–40% relative humidity conditions. Once the samples were cool down, thiazolium iodide salt were dropped on perovskite layers for spin-coating at 3500 r.p.m for 30 s and kept at 100 °C for 10 min. When samples reach room temperature, Spiro-OMeTAD was then spun coated at 4000 rpm for 30 s by dissolving 72.3 mg of Spiro-OMeTAD in 1 ml of chlorobenzene; 28.8 ml of 4-tert-butylpyridine was added to the solution as dopants. Finally, 70 nm of gold was deposited by thermal evaporation.

*Synthesis of thiazole salt*

4-methylthiazole and 4,5-dimethylthiazole. In a round bottom flask, 239 mg of thiazole (2,8 mmol, 1 equiv.) were dissolved in 1 mL of MeOH, then 2.28 g of MeI (16 mmol, 5.7 equiv.) were added and the solution was stirred at room temperature for 36 hours under dark. The product was precipitated with 5 mL of AcOEt and the filtrated was washed with 2×10 mL of AcOEt. The powder was dried under reduced pression, affording the desired product as a white solid {yield= 78.8% (MIC2), 61% (MIC3), 93% (MIC4)}. ^{1}H in DMSO-$d_6$ and ^{13}C NMR in $CD_3OD$ spectra of compounds MIC2- MIC3- MIC4 were recorded and are presented in Figure S1 (Supporting Information).

**$N$-methylthiazolium Iodide (1)**: ^{1}H NMR (500 MHz, DMSO) δ 10.10 (m, 1H), 8.46 (dd, $J$ = 3.6, 1.2 Hz, 1H), 8.30 (dd, $J$ = 3.6, 2.6 Hz, 1H), 4.20 (s, 3H). ^{13}C NMR (125 MHz, MeOD) δ 160.2 (s), 139.5 (s), 127.1 (s), 42.6 (s).

**3,4-dimethyl thiazolium iodide (2)**- ^{1}H NMR (500 MHz, DMSO) δ 10.05 (d, $J$ = 2.4 Hz, 1H), 7.97 (m, 1H), 4.08 (s, 3H), 2.51 (s, overlapping DMSO, 3H). ^{13}C NMR (125 MHz, MeOD) δ 160.1 (s), 148.5 (s), 122.2 (s), 40.9 (s), 13.5 (s).

**3,4,5-trimethyl thiazolium iodide (3)**. ^{1}H NMR (500 MHz, DMSO) δ 9.92 (s, 1H), 4.07 (s, 3H), 2.49 (s, 3H), 2.40 (s, 3H). ^{13}C NMR (125 MHz, MeOD) δ 156.0 (s), 144.0(s), 134.4 (s), 41.4 (s), 12.4 (s), 11.6 (s).


*Thin film Characterization*

For structural characterization, thin films were prepared by spin coating of $MAPbI_3$ and $MAPbI_3$ + thiazolium solutions onto glass. X-ray diffractograms were recorded using a D8 Advance diffractometer from Bruker (Bragg-Brentano geometry, with an X-ray tube Cu Kα, λ=1.5406 Å). A scan range of 3 – 80° was selected with an acquisition time of 1 degree per min. For XRD-temperature dependence, perovskite film was deposited on an aluminium substrate to facilitate a homogeneous distribution of the temperature. The absorption spectra were registered with an UV–Vis–IR spectrophotometer (Varian Cary 50 UV/Vis Spectrophotometer).

Photoluminescence (PL) steady-state measurements were recorded with a spectrophotometer (PerkinElmer Instrument LS55). The femtosecond transient absorption spectrometer is described elsewhere.[44] Ultrashort laser pulses were generated in an oscillator-regenerative amplifier laser system (Coherent, Mantis-Legend) that provides a 1 KHz train of 35 fs pulses at 800 nm. Pump pulse wavelength in the range 500 nm-650 nm is obtained by means of sum frequency of the fundamental 800 nm and the signal beam of an optical parametric amplifier (Coherent, TOPAS) while the 400 nm is generated as the second harmonic of the fundamental beam. The white light continuum probe is produced by focusing (f =100 mm) a small fraction of the amplifier output on a 2 mm thick $CaF_2$ window. Pump probe delay is achieved with a translation stage (Thorlabs, DDS220) that allows a maximum range of 1 ns. Transient absorbance was measured with a fiber-coupled spectrometer (Avantes, Avaspec) as a function of the pump probe delay. Samples were continuously scanned across the focal plane to avoid thermal effects on the sample. The spot radii of the pump and probe pulses (0.55 mm and 0.2 mm) at sample surface were measured by means of a CMOS camera. Pump pulse energies were varied in the range 20 nJ – 200 nJ.

*Device characterization*

Current density–voltage (*J–V*) curves were recorded using an Oriel solar simulator (Newport) producing 1 sun AM 1.5 (1000 $W/m^2$) sunlight. Current-voltage curves were measured in air with a potentiostat (Keithley 2604). *J-V* measurement were performed at 100 mV $s^{-1}$ scan rate (pre sweep delay: 10 s) and a black metal mask (0.16 $cm^2$) was used over the square solar cell active area to reduce the influence of scattered light. Incident photon current efficiency (IPCE) measurements were carried out using a 150W Xenon lamp attached to with Bentham PVE300 motorized 1/4m monochromator as the light source. Impedance Spectroscopy (IS) measurements were carried out altering the positions of the Fermi level by a white LED source. During the measurements, samples were kept inside a faradaic chamber to avoid external interferences. A 20 mV perturbation in the range 2MHz–1mHz was used to obtain the spectra. After measurement, data were fitted by Z-view software and analysed in order to extract characteristic parameters of the cells.

**Supplementary Information**

Supplemental information includes Figure S1-S14, and can be found with this article online at

**Acknowledgements**

**Author Contributions**

MSM made the experiments, devices, impedance spectroscopy and collected the data, MA synthesized the thiazolium salts, MA and FC ran the *ab-initio* computational studies, PH fabricated effective performance devices, TK perform admittance spectroscopy and data analysis, SK performed electro-optical and spectroscopy measurements. S.A supervised and directed the research. All authors contributed to the first draft and commented to the completion of the final document.

**Conflict of Interests**

The authors declare no competing interests.

*References*

[1]     "NREL Efficiency Chart. http://www.nrel.gov/ncpv/images/ efficiency_chart.jpg," **n.d.**

[2]     N. J. Jeon, J. H. Noh, W. S. Yang, Y. C. Kim, S. Ryu, J. Seo, S. Il Seok, *Nature* **2015**, *517*, 476.

[3]     G. Grancini, I. Zimmermann, E. Mosconi, D. Martineau, S. Narbey, *Nat. Commun.* **2017**, *8*, 1.

[4]     M. Saliba, T. Matsui, J.-Y. Seo, K. Domanski, J.-P. Correa-Baena, M. K. Nazeeruddin, S. M. Zakeeruddin, W. Tress, A. Abate, A. Hagfeldt, M. Grätzel, *Energy Environ. Sci.* **2016**, *9*, 1989.

[5]     A. J. Knight, A. D. Wright, J. B. Patel, D. P. McMeekin, H. J. Snaith, M. B. Johnston, L. M. Herz, *ACS Energy Lett.* **2019**, *4*, 75.

[6]     S. Heo, G. Seo, Y. Lee, M. Seol, S. H. Kim, D. J. Yun, Y. Kim, K. Kim, J. Lee, J. Lee, W. S. Jeon, J. K. Shin, J. Park, D. Lee, M. K. Nazeeruddin, *Adv. Mater.* **2019**, *31*, 1.

[7]     M. Lira-Cantú, *Nat. Energy* **2017**, *2*, 17115.

[8]     R. E. Beal, D. J. Slotcavage, T. Leijtens, A. R. Bowring, R. A. Belisle, W. H. Nguyen, G. Burkhard, E. T. Hoke, M. D. McGehee, *J. Phys. Chem. Lett.* **2016**, *7*, 746.

[9]     M. Stolterfoht, P. Caprioglio, C. M. Wolff, J. A. Márquez, J. Nordmann, S. Zhang, D. Rothhardt, U. Hörmann, A. Redinger, L. Kegelmann, S. Albrecht, T. Kirchartz, M. Saliba, T. Unold, D. Neher, **2018**.

[10]    M. Salado, A. D. Jodlowski, C. Roldan-Carmona, G. de Miguel, S. Kazim, M. K. Nazeeruddin, S. Ahmad, *Nano Energy* **2018**, *50*, 220.

[11]    X. Li, S. P. Lau, L. Tang, R. Ji, P. Yang, *Nanoscale* **2014**, *6*, 5323.

[12]    J. J. Choi, X. Yang, Z. M. Norman, S. J. L. Billinge, J. S. Owen, *Nano Lett.* **2014**, *14*, 127.

[13]    L. Gao, I. Spanopoulos, W. Ke, S. Huang, I. Hadar, L. Chen, X. Li, G. Yang, M. G. Kanatzidis, *ACS Energy Lett.* **2019**, *4*, 1763.

[14]    S. F. Hoefler, G. Trimmel, T. Rath, *Monatshefte fur Chemie* **2017**, *148*, 795.

[15]    W. Q. Liao, H. Y. Ye, Y. Zhang, R. G. Xiong, *Dalt. Trans.* **2015**, *44*, 10614.

[16]    Q. Jiang, Y. Zhao, X. Zhang, X. Yang, Y. Chen, Z. Chu, Q. Ye, X. Li, Z. Yin, J. You, *Nat. Photonics* **2019**, *13*, 460.

[17]    J. J. Yoo, S. Wieghold, M. C. Sponseller, M. R. Chua, S. N. Bertram, N. T. P. Hartono, J. S. Tresback, E. C. Hansen, J.-P. Correa-Baena, V. Bulović, T. Buonassisi, S. S. Shin, M. G. Bawendi, *Energy Environ. Sci.* **2019**, *12*, 2192.

[18] M. Salado, M. A. Fernández, J. P. Holgado, S. Kazim, M. K. Nazeeruddin, P. J. Dyson, S. Ahmad, *ChemSusChem* **2017**, *10*, 3846.

[19] Y. Liu, S. Akin, L. Pan, R. Uchida, N. Arora, J. V. Milić, A. Hinderhofer, F. Schreiber, A. R. Uhl, S. M. Zakeeruddin, A. Hagfeldt, M. I. Dar, M. Grätzel, *Sci. Adv.* **2019**, *5*, 2543.

[20] T. A. Berhe, W.-N. Su, C.-H. Chen, C.-J. Pan, J.-H. Cheng, H.-M. Chen, M.-C. Tsai, L.-Y. Chen, A. A. Dubale, B.-J. Hwang, *Energy Environ. Sci.* **2016**, *9*, 323.

[21] Y.-Y. Zhang, S. Chen, P. Xu, H. Xiang, X.-G. Gong, A. Walsh, S. Wei, *Chinese Phys. Lett.* **2015**, *35*, 11.

[22] X. Huang, H. Guo, K. Wang, X. Liu, *Org. Electron. physics, Mater. Appl.* **2017**, *41*, 42.

[23] Z. Li, J. Dong, C. Liu, J. Guo, L. Shen, W. Guo, *Nano-Micro Lett.* **2019**, *11*, 50.

[24] Y. Shao, Z. Xiao, C. Bi, Y. Yuan, J. Huang, *Nat. Commun.* **2014**, *5*, 5784.

[25] K. Chen, Q. Hu, T. Liu, L. Zhao, D. Luo, J. Wu, Y. Zhang, W. Zhang, F. Liu, T. P. Russell, R. Zhu, Q. Gong, *Adv. Mater.* **2016**, *28*, 10718-10724.

[26] C. Sun, Z. Wu, H. L. Yip, H. Zhang, X. F. Jiang, Q. Xue, Z. Hu, Z. Hu, Y. Shen, M. Wang, F. Huang, Y. Cao, *Adv. Energy Mater.* **2016**, *6*, 1501534.

[27] D. W. DeQuilettes, S. M. Vorpahl, S. D. Stranks, H. Nagaoka, G. E. Eperon, M. E. Ziffer, H. J. Snaith, D. S. Ginger, *Science.* **2015**, *348*, 683.

[28] N. K. Noel, A. Abate, S. D. Stranks, E. S. Parrott, V. M. Burlakov, A. Goriely, H. J. Snaith, *ACS Nano* **2014**, *8*, 9815.

[29] N. Aristidou, C. Eames, I. Sanchez-Molina, X. Bu, J. Kosco, M. Saiful Islam, S. A. Haque, *Nat. Commun.* **2017**, *8*, 15218.

[30] G. Xing, N. Mathews, S. Sun, S. S. Lim, Y. M. Lam, M. Gra̋zel, S. Mhaisalkar, T. C. Sum, *Science (80).* **2013**, *342*, 344.

[31] P. Piatkowski, B. Cohen, F. Javier Ramos, M. Di Nunzio, M. K. Nazeeruddin, M. Grätzel, S. Ahmad, A. Douhal, *Phys. Chem. Chem. Phys.* **2015**, *17*, 14674.

[32] P. Piatkowski, B. Cohen, C. S. Ponseca, M. Salado, S. Kazim, S. Ahmad, V. Sundström, A. Douhal, *J. Phys. Chem. Lett.* **2016**, *7*, 204.

[33] I. Zarazua, J. Bisquert, G. Garcia-Belmonte, *J. Phys. Chem. Lett.* **2016**, *7*, 525.

[34] E. Von Hauff, *J. Phys. Chem. C* **2019**, *123*, 11329−11346.

[35] L. Contreras-Bernal, S. Ramos-Terrón, A. Riquelme, P. P. Boix, J. Idígoras, I. Mora-Seró, J. A. Anta, *J. Mater. Chem. A* **2019**, *7*, 12191.

[36] O. Almora, K. T. Cho, S. Aghazada, I. Zimmermann, G. J. Matt, C. J. Brabec, M. K. Nazeeruddin, G. Garcia-Belmonte, *Nano Energy* **2018**, *48*, 63.

[37] J. Zhang, Z. Jin, L. Liang, H. Wang, D. Bai, H. Bian, K. Wang, Q. Wang, N. Yuan, J. Ding, S. (Frank) Liu, *Adv. Sci.* **2018**, *5*, 1801123.

[38] M. T. Khan, M. Salado, A. Almohammedi, S. Kazim, S. Ahmad, *Adv. Mater. Interfaces* **2019**, *6*, 1901193.

[39] Q. Chen, L. Chen, F. Ye, T. Zhao, F. Tang, A. Rajagopal, Z. Jiang, S. Jiang, A. K. Y. Jen, Y. Xie, J. Cai, L. Chen, *Nano Lett.* **2017**, *5*, 3231-3237.

[40] N. Li, S. Tao, Y. Chen, X. Niu, C. K. Onwudinanti, C. Hu, Z. Qiu, Z. Xu, G. Zheng, L. Wang, Y. Zhang, L. Li, H. Liu, Y. Lun, J. Hong, X. Wang, Y. Liu, H. Xie, Y. Gao, Y. Bai, S. Yang, G. Brocks,

Q. Chen, H. Zhou, *Nat. Energy* **2019**, *4*, 408.

[41]  P. Mark, W. Helfrich, *J. Appl. Phys.* **1962**, *33*, 205.

[42]  M. A. L. and P. Mark, *Acad. New York* **1970**, DOI 10.1088/0031-9112/21/12/031.

[43]  K. C. Kao and W. Hwang, *Pergamon Oxford* **1981**, *32*, 258.

[44]  R. Losantos, I. Lamas, R. Montero, A. Longarte, D. Sampedro, *Phys. Chem. Chem. Phys.* **2019**, *21*, 11376.